Bioactive Materials 5 (2020) 377–386

Contents lists available at ScienceDirect

Bioactive Materials

journal homepage: http://www.keaipublishing.com/biomat

Enhanced physicochemical and biological properties of C/Cu dual ions implanted medical titanium

Chao Xia[a,b], Xiaohan Ma[a,d], Xianming Zhang[a,c], Kunqiang Li[a,b], Ji Tan[a,b], Yuqin Qiao[a,d,**], Xuanyong Liu[a,b,d,*]

[a] State Key Laboratory of High Performance Ceramics and Superfine Microstructure, Shanghai Institute of Ceramics, Chinese Academy of Sciences, Shanghai, 200050, China
[b] Center of Materials Science and Optoelectronics Engineering, University of Chinese Academy of Sciences, Beijing, 100049, China
[c] Shanghai Normal University, Shanghai, 200234, China
[d] Cixi Center of Biomaterials Surface Engineering, Shanghai Institute of Ceramics, Chinese Academy of Sciences, Ningbo, 315300, China

ARTICLE INFO

Keywords:
Titanium
Ion implantation
Carbon
Copper
Antibacterial ability

ABSTRACT

It is increasingly popular for titanium and its alloys to be utilized as the medical implants. However, their bioinert nature and lack of antibacterial ability limit their applications. In this work, by utilizing plasma immersion ion implantation and deposition (PIII&D) technology, the titanium surface was modified by C/Cu co-implantation. The mechanical property, corrosion resistance, antibacterial ability and cytocompatibility of modified samples were studied. Results indicate that after C/Cu co-implantation, copper nanoparticles were observed on the surface of titanium, and titanium carbide existed on the near surface region of titanium. The modified surface displayed good mechanical property and corrosion resistance. The Cu/C galvanic corrosion existed on the titanium surface implanted by C/Cu dual ions, and release of copper ions can be effectively controlled by the galvanic corrosion effect. Moreover, improved antibacterial performance of titanium surface can be achieved without cytotoxicity.

1. Introduction

Nowadays, the number of patients with osteoarthrosis and the demand for artificial joints are growing because of faster aging population [1,2]. It is more popular for titanium and its alloys used as artificial joint materials [3–5]. However, the biological activity of the titanium materials is not ideal to combine with the surrounding tissue in a short time [6,7]. In addition, an oxide passivation film is usually formed on the titanium surface, which may be peeled off and dissolved under the influence of external force and body fluid [8,9]. This may cause toxicity, inflammation, and thrombosis in the body, so the corrosion resistance of titanium needs to be improved. Furthermore, titanium surface lacks antibacterial ability, which may cause postoperative bacterial infection, eventually leading to surgical failure [10]. Thus, it is important to modify titanium surface to improve its biological activity, mechanical property, corrosion resistance and antibacterial ability.

A diamond-like carbon film is an amorphous carbon film with performances similar to those of a diamond film. Owing to good corrosion resistance, wear resistance and biocompatibility, DLC film has been obtained great attention in the field of biomedicine, especially artificial joints for more than 10 years [11–13]. There are various ways to prepare DLC films, including CVD (chemical vapor deposition) [14], PVD (physical vapor deposition) [15], and PIII&D (plasma immersion ion implantation and deposition) [16,17]. Compared to CVD and PVD, PIII&D technology has some unique features. It has the advantages of full-scale implantation, surface reaction, high reactivity of the injected component, and no distinct interface exists between the substrate and the modified layer [18,19]. By using this technology and controlling process parameters, carbon ions can be implanted into titanium and its alloys to form TiC or DLC modified layer on their surfaces to improve mechanical property and corrosion resistance [20–22].

However, the surface of the C-implanted titanium in our previous

Peer review under responsibility of KeAi Communications Co., Ltd.
* Corresponding author. State Key Laboratory of High Performance Ceramics and Superfine Microstructure, Shanghai Institute of Ceramics, Chinese Academy of Sciences, Shanghai, 200050, China.
** Corresponding author. State Key Laboratory of High Performance Ceramics and Superfine Microstructure, Shanghai Institute of Ceramics, Chinese Academy of Sciences, Shanghai, 200050, China.
E-mail addresses: qiaoyq@mail.sic.ac.cn (Y. Qiao), xyliu@mail.sic.ac.cn (X. Liu).

https://doi.org/10.1016/j.bioactmat.2020.02.017
Received 2 February 2020; Received in revised form 28 February 2020; Accepted 28 February 2020

research cannot inhibit bacterial growth well enough [23]. Amorphous carbon can only interact with those bacteria adhered on its surface, so the interaction between amorphous carbon and bacteria is weak [26,27]. Copper (Cu) is an essential micronutrient which has received increasing attention because of its role in wound healing, angiogenesis and antibacterial activities [24,25]. Cu ions released tend to interact in a wide range with cells or bacteria. Thus, co-implantation of C and Cu into titanium, may produce better antibacterial ability than single Cu implantation, which combined both antibacterial effects of carbon and copper ions.

In this work, titanium surface is modified by C/Cu dual ions implantation using PIII&D technology. Mechanical property, corrosion resistance, antibacterial ability and cytotoxicity of implanted samples are investigated.

2. Materials and methods

2.1. C/Cu ions implantation

Commercial pure titanium plates were cut into samples with the sizes of 10 mm × 10 mm × 1 mm and 20 mm × 10 mm × 1 mm , and then those samples were pretreated with mixed acid (HF and HNO_3), before being ultra-sonicated with alcohol and ultrapure water in sequence. The samples were placed in a target table of PIII&D vacuum chamber, Carbon target was high-purity graphite rod (99.99%, 10 × 28 mm), and copper target was high-purity copper rod (99.99%, 10 × 28 mm). Vacuum was pulled below 5×10^{-3} Pa, and then carbon and copper implantation or carbon/copper dual ions implantation were conducted for 1 h, and parameters of implantation are displayed in Table 1. Samples with carbon implantation were represented by C–Ti; samples with copper implantation were represented by Cu–Ti, and samples with carbon/copper ions co-implantation were represented by C/Cu–Ti.

2.2. Surface characterization

A field emission scanning electron microscope (FE-SEM; S-4800, Hitachi, Japan) was harnessed to observe surface morphologies of samples. The surface element composition of samples was probed by X-ray photoelectron spectroscopy (XPS; Physical electronics PHI-5802, PHI, USA), and XPS high-resolution spectrum was used to analyze the chemical states of elements.

2.3. Wettability of surfaces

A contact angle meter (SL200B, Solon, China) was utilized to analyze the wettability of surfaces. 2 μL of ultrapure water was dropped vertically on samples' surfaces. Then, the contact angle of the droplet was measured.

2.4. Surface zeta potential

A surpass electric analyzer was utilized to detect the zeta potential (ζ) of surface. Two samples with the size of 20 × 10 × 1 mm^3 were placed on the stage, and the distance of gap between two parallel samples was adjusted to 100 ± 5 μm to ensure that the electrolyte (0.001 mol/L KCl solution) passed through the gap. HCl and NaOH solutions were added to change pH value of the electrolyte in the range of 5.0–9.0. The current and pressure on the sample' surface were measured at a certain pH value, and Helmholtz-Smoluchowski formula was adopted to calculate the value of zeta potential (ζ) [28]:

$$\zeta = \frac{dI}{dP} \times \frac{\eta}{\varepsilon \times \varepsilon_0} \times \frac{L}{A} \quad (1)$$

where A and L are the cross-sectional area and length of the electrolyte channel, respectively; η, ε, ε_0 are the viscosity of the electrolyte, the dielectric constant and the vacuum dielectric constant respectively; dI/dP is the slope of the flow current versus pressure change.

Table 1
Parameters used for C/Cu plasma immersion ions implantation & deposition (PIII&D).

	C–Ti	Cu–Ti	C/Cu–Ti
Implantation voltage (kV)	−30	−30	−30
Implantation pulse duration (μs)	1000	1000	1000
Pulsing frequency (Hz)	8	8	8

2.5. Cu^{2+} release

C/Cu–Ti and Cu–Ti were placed in centrifuge tubes with 10 mL of PBS and these tubes were placed in a 37 °C incubator. An inductively coupled plasma atomic emission spectroscopy (ICP-AES) was used to determine the amounts of released copper ions (1, 4, 7, and 14 days).

2.6. Test of electrochemical performance

A CHI760C electrochemical workstation was used to test the corrosion resistance of different samples. The working electrode was a test sample, and a graphite electrode acted as the counter electrode, while a saturated calomel electrode serveed as the reference electrode. The electrolyte used in this test was 0.9 wt% NaCl solution, and the Tafel curve of each sample was measured at room temperature, and the scanning rate was set to 0.01 V/s.

2.7. Hardness of surface

A G200 nano-indenter was harnessed to measure the micro-hardness value of the test sample's surface, meanwhile the hardness was measured by selecting 3 points on each sample.

2.8. Test of antibacterial ability

By using *S. aureus* (ATCC 25923) and *E. coli* (ATCC 25922), the antibacterial ability of samples modified through ion implantation was evaluated. After sterilized under light of ultraviolet for 24 h, samples were put into a 24-well plate, and 100 μL of bacterial liquid with a bacterial concentration of 10^6 cfu/mL was added to each sample's surface. Bacteria on various surfaces were then cultured in a 37 °C incubator for 24 h, before being quickly transferred to centrifuge tubes containing 4 mL of physiological saline, and these tubes were shaken vigorously on a shaker for 30 s to detach the bacteria from the sample. Afterwards, the isolated bacterial suspensions were sequentially diluted 10 times in the sterilized physiological saline, and then 100 μL of the diluted bacterial solutions were uniformly applied to standard agar plates (Nutrient Broth No. 2 (NB) for *S. aureus* and Luria-Bertani (LB) for *E. coli*). After cultured for 16 h in a 37 °C incubator, the agar plates were removed from the incubator to count the number of colonies, and the antibacterial rate of the sample was calculated by using the following formula:

$$k = \frac{A - B}{A} \times 100\% \quad (2)$$

K: sample antibacterial rate.
A: Number of colonies in the control sample.
B: Number of colonies in the experimental group.

Besides, an additional sample was added to each culture group to observe the microscopic morphology and number of bacteria under a scanning electron microscope (SEM).

2.9. Cytotoxicity evaluation

Cytotoxicity of each sample was evaluated by using mouse osteoblast cells (MC3T3-E1). The MC3T3-E1 cells with a density of 2×10^4 cells/mL were seeded on the surfaces of samples, and every 3 days the culture solution was changed. After 1, 4, and 7 days, an original culture medium was aspirated, and a fresh culture medium which contained 10% alamarBlue™ was added. At the end of incubation, 100 μL of the medium was pipetted from each well into a black 96-well plate (Nunc, USA). And the intensity of fluorescence was measured in a condition where the wavelengths of excitation and emission were 550 nm and 590 nm, respectively.

2.10. Statistical analysis

Experimental data were statistically analyzed by means of GraphPad Prism software. Differences between experimental variables in different groups were analyzed by one-way ANOVA and Tukey's multi-group comparison experiments. Each set of variables contained at least three valid values, and the significance difference level was set to $p = 0.05$. If $p < 0.05$, a statistically significant difference existed.

3. Result and discussion

3.1. Surface characterization

Fig. 1 shows surface morphologies of samples before and after ions implantation. There was gully-shaped structure formed by mixed acid processing, and the surface morphologies of samples did not have obvious change after ion implantation (Fig. 1a–d). However, through observation from high-magnification images (Fig. 1e–h), both Cu–Ti and C/Cu–Ti surfaces contained nano-particles, which were formed due to process of Cu-PIII&D [29,30].

Atomic percentages of elements in 30 nm depth of samples analyzed though XPS are shown in Table 2. According to this table, carbon and copper ions have been successfully implanted into the modified substrates. Exactly, carbon relative atomic percentages of C–Ti and C/Cu–Ti were about 13.78 at.% and 10.04 at.%, respectively, while the copper relative atomic percentages of Cu–Ti and C/Cu–Ti were about 11.84 at.% and 13.68 at.%, respectively.

C 1s high-resolution XPS on surfaces and at 30 nm depth of C–Ti and C/Cu–Ti are displayed in Fig. 2a–d. As shown from Fig. 2a, there were four fitting peaks in C 1s high-resolution spectrum on surface of the C–Ti, main peak at 284.30 eV corresponded to C 1s binding energy in amorphous carbon [31], and double peaks at 285.70 eV and 281.50 eV corresponded to C 1s binding energy in graphite [32] and titanium carbide, [33] respectively. The peak at 288.00 eV corresponded to C = O chemical bond [34]. Fig. 2c shows C 1s high-resolution spectrum at 30 nm depth of C–Ti sample, and single peak at 281.50 eV corresponded to C 1s binding energy in titanium carbide [33]. C 1s peak on surface of the C/Cu–Ti sample (Fig. 2b) was located at 284.31 eV and 288.00 eV corresponding to C 1s binding energy in amorphous carbon and C = O chemical bond. C 1s high-resolution spectrum (Fig. 2d) of C/Cu-Ti at 30 nm depth was located at 281.50 eV, corresponding to C 1s binding energy in titanium carbide [33]. These results indicate carbon elements existed in C/Cu–Ti and C–Ti as titanium carbide and existed on the surfaces of these two samples in the form of amorphous carbon. XPS high-resolution spectra of Cu 2p from surfaces and inside of Cu–Ti and C/Cu–Ti at 30 nm depth are exhibited in Fig. 2e–h. There were six fitting peaks in Cu–Ti surface's Cu 2p high-resolution spectrum in Fig. 2e, where double peaks at 952.45 eV and 932.00 eV corresponded to Cu $2p_{1/2}$ and Cu $2p_{3/2}$ binding energies in metallic Cu, respectively [35,36], double peaks at 954.00 eV and 934.20 eV corresponded to Cu $2p_{1/2}$ and Cu $2p_{3/2}$ binding energies in copper oxide, respectively [37]. In addition, characteristic peaks occurred at 962.00 and 941.90 eV corresponded to satellite peaks of CuO [38,39].

Table 2
XPS atomic percentages of elements at 30 nm depth of samples.

Element (at.%)	C–Ti	Cu–Ti	C/Cu–Ti
C1s	13.78	–	10.04
Cu2p	–	11.84	13.68
O1s	40.35	53.88	44.12
Ti2p	45.87	34.28	32.17

XPS high-resolution spectrum of Cu 2p gained from the inside of Cu–Ti at 30 nm depth is shown in Fig. 2g, where double peaks were located at 952.45 eV and 932.63 eV, corresponding to Cu $2p_{1/2}$ and Cu $2p_{3/2}$ binding energies of metallic Cu, respectively [40,41]. The high resolution Cu 2p spectra of C/Cu-Ti on surface is similar to that of Cu-Ti (Fig. 2f). Double peaks (Fig. 2h) of Cu 2p at 30 nm depth were positioned at 952.45 eV and 932.67 eV respectively, which corresponded to Cu $2p_{1/2}$ and Cu $2p_{3/2}$ binding energies of metallic Cu respectively [41,42]. The above results indicate copper existed on both surface and inside of C/Cu–Ti and C–Ti.

Ti 2p high-resolution XPS on surfaces and inside of different samples are displayed in Fig. 3. As shown from Fig. 3a, there were four fitting peaks in Ti 2p high-resolution spectrum on surface of the C–Ti. Two main peaks located at 458.20 eV and 464.19 eV, corresponding to Ti $2p_{3/2}$ and Ti $2p_{1/2}$ binding energies in TiO_2, respectively [43,44]. And two peaks at 462.00 eV and 455.90 eV corresponded to Ti $2p_{1/2}$ and Ti $2p_{3/2}$ in Ti_2O_3[45,46], respectively. Fig. 3b shows high-resolution spectrum of Ti 2p at 30nm depth of C-Ti and six peaks can be found. Two main peaks were located at 454.20 eV and 460.20 eV corresponding to Ti $2p_{3/2}$ and Ti $2p_{1/2}$ binding energies of Ti-C [47,48]. Peaks at 456.10 eV and 461.50 eV corresponded to Ti $2p_{3/2}$ and Ti $2p_{1/2}$ binding energies of Ti^{2+} respectively [49,50]. Two peaks located at 457.73 eV and 463.52 eV presented Ti $2p_{3/2}$ and Ti $2p_{1/2}$ binding energies of TiO_2 respectively [51].

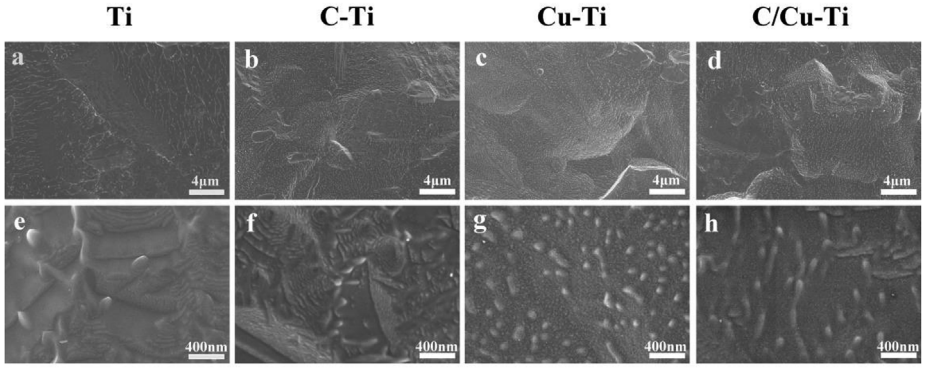

Fig. 1. Morphology of surfaces at low magnification (a-d) and high magnification (e-f).

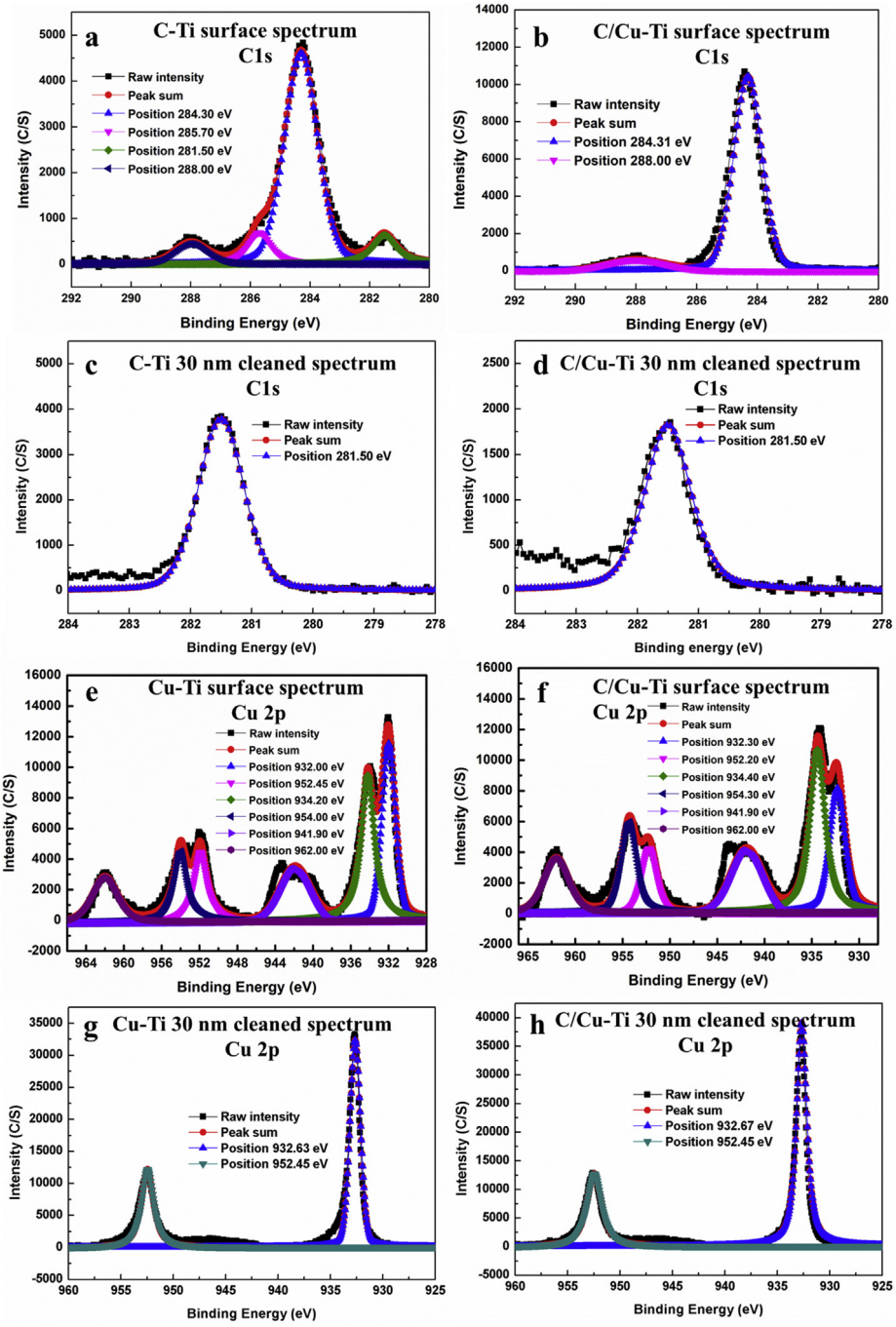

Fig. 2. C1s XPS high-resolution spectra gained from C–Ti and C/Cu–Ti surfaces (a and b) and inside at 30 nm depth (c and d); Cu 2p XPS high-resolution spectra gained from Cu–Ti and C/Cu–Ti surfaces (e and f) and inside at 30 nm depth (g and h).

Ti 2p peaks on surface of Cu–Ti were situated at 458.33 eV and 464.19 eV, corresponding to Ti $2p_{3/2}$ [52] and Ti $2p_{1/2}$ [44] binding energies of TiO_2 (Fig. 3c). There were six peaks in Ti 2p high-resolution spectrum of Cu-Ti at 30 nm depth (Fig. 3d). Two peaks were located at 454.70 eV and 460.20 eV corresponding to Ti $2p_{3/2}$ and Ti $2p_{1/2}$ binding energies of metallic Ti [53,54]. It has been reported that Ti $2p_{3/2}$ and Ti $2p_{1/2}$ peaks (about 454 eV and 460 eV) of Ti-C overlapped with those of pure Ti [55,56]. Thus, we resolve these peaks according to specific experiments and C 1s high resolution of samples. Two peaks situated at 458.06 eV and 463.65 eV corresponded to Ti $2p_{3/2}$ and Ti $2p_{1/2}$ binding energies of TiO_2 respectively [57]. The other two peaks which were positioned at 456.52 eV and 462.00 eV corresponded to Ti^{3+} [58].

Ti 2p high-resolution spectrum on surface of C/Cu–Ti is shown in Fig. 3e. Two peaks located at 458.20 eV and 464.00 eV corresponded to binding energies of Ti $2p_{3/2}$ and Ti $2p_{1/2}$ in TiO_2 [59]. Fig. 3f displays high-resolution spectrum of Ti 2p at 30nm depth of C/Cu-Ti. Two peaks at 454.20 eV and 460.00 eV corresponded to Ti $2p_{3/2}$ and Ti $2p_{1/2}$ binding energies of Ti-C [48]. Double peaks at 457.73 eV and 463.52 eV corresponded to Ti $2p_{3/2}$ and Ti $2p_{1/2}$ binding energies of TiO_2 [51]. The other two peaks at 456.10 eV and 461.50 eV corresponded to Ti^{2+} [49,50].

These results indicate titanium element mainly existed on C–Ti, Cu–Ti and C/Cu–Ti in the form of TiO_2, while it mainly existed as titanium carbide and/or pure titanium at the depth of 30 nm inside C–Ti, Cu–Ti and C/Cu–Ti.

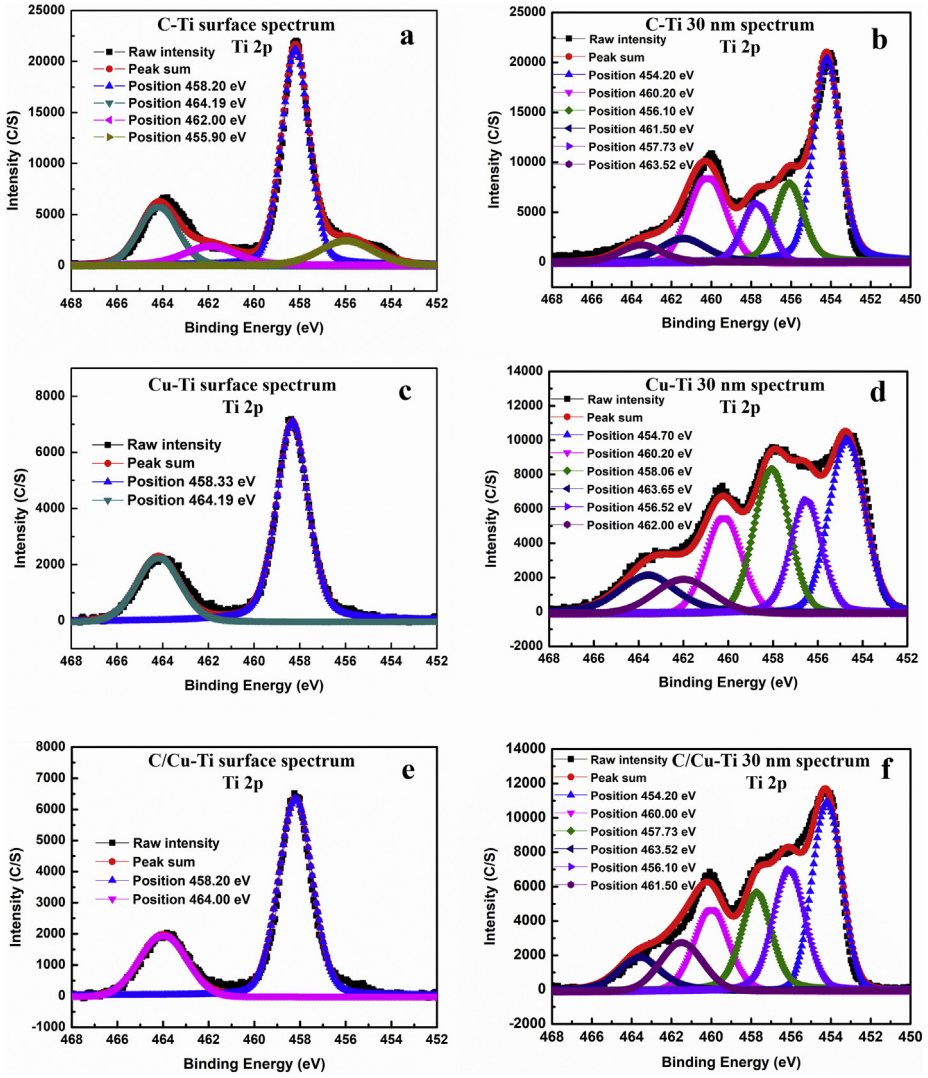

Fig. 3. XPS high-resolution spectra of Ti 2p obtained from surfaces (a, c and e) and inside of C–Ti, Cu–Ti and C/Cu–Ti at 30 nm depth (b, d and f).

3.2. Surface wettability

The measured water contact angles of different samples are shown in Fig. 4. Ti, C–Ti, Cu–Ti and C/Cu–Ti samples' contact angles were 52.5 ± 4.0°, 46.6 ± 3.6°, 50.7 ± 2.4° and 49.6 ± 1.3° respectively. There is no obvious difference among these groups, indicating that the surface wettability could not be changed by ion implantation.

Fig. 5 displays the release curves of Cu^{2+} of Cu–Ti and C/Cu–Ti

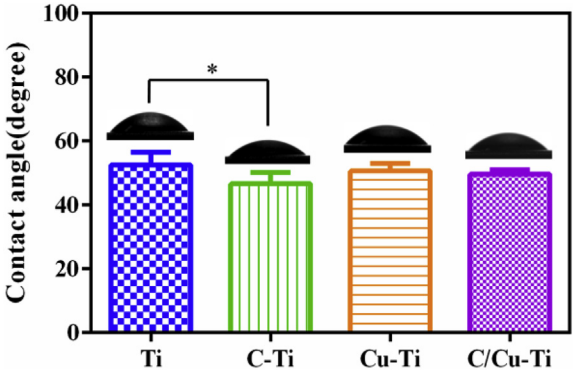

Fig. 4. Water contact angles measured from various surfaces.

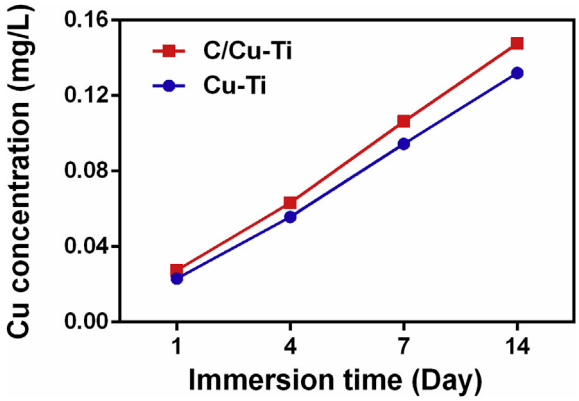

Fig. 5. Cu^{2+} release curves from Cu–Ti and C/Cu–Ti immersed in PBS for two weeks.

immersed in PBS for two weeks. It can be seen that as the immersion time extended, Cu^{2+} concentration was increased. And the amount of copper ions released from C/Cu–Ti was more than that from Cu–Ti.

Fig. 6 and Table 3 show curves of polarization and relevant data of samples in physiological saline before and after modification. The corrosion potentials of modified samples (C–Ti, Cu–Ti and C/Cu–Ti) all

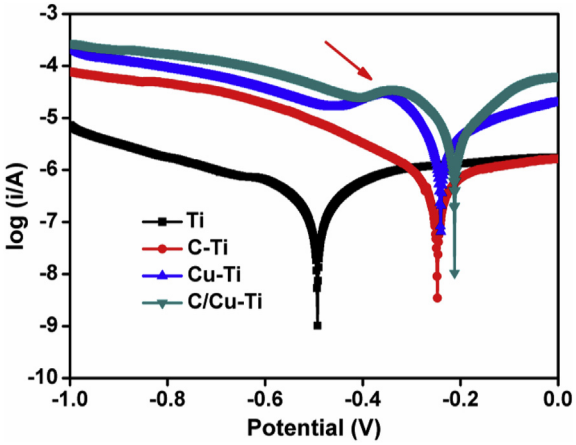

Fig. 6. Polarization curves of various samples.

Table 3
Corrosion potentials and currents of various samples.

	Ti	C–Ti	Cu–Ti	C/Cu–Ti
E_{corr} (V) *vs.* SCE	−0.489	−0.247	−0.239	−0.213
I_{corr} (A cm^{-2})	2.630×10^{-7}	7.943×10^{-7}	3.981×10^{-6}	3.459×10^{-6}

showed positive shift (shown by the red arrow), indicating anticorrosion performances of modified samples were improved. Anticorrosion performance of C–Ti was improved due to amorphous carbon formed on surface and TiC inside C–Ti [20,22].

After copper ions implantation, copper oxide existed on Cu–Ti. It has been reported that copper oxide had good corrosion resistance [60], thus the corrosion potential of Cu–Ti could be larger than that of Ti surface. The reason why the corrosion resistance of titanium surface can be enhanced by C/Cu co-implantation may be that the standard electrode potential of nano-scale TiO_2 film was −0.502 V [61], and the standard electrode potential of Cu is +0.34 V [29], while amorphous carbon with stable chemical properties existed on the surface. The amorphous carbon film has an amorphous metastable structure containing sp^2 carbon and sp^3 carbon [62]. Amorphous carbon contains a certain amount of free electrons from the sp^2 hybrid, so it has conductive property. Owing to low electron affinity and chemical inertness, amorphous carbon is a strong candidate for cathode [63].

According to the corrosion principle of electrochemistry, a C/Cu galvanic corrosion pair could be formed in a liquid environment. Cu would preferentially act as the anode where Cu^{2+} ions were relesed, while C would be the cathode, and the TiO_2 layer was the path of electronic transmission. As a result of the above reaction, the Ti substrate was protected and the corrosion resistance was improved.

The specific reactions take below:

$$\text{Cu (anode): } Cu \rightarrow Cu^{2+} + 2e^- \quad (5)$$

$$\text{C (cathode): } 2H^+ + 2e^- \rightarrow H_2 \quad (6)$$

$$O_2 + 4H^+ + 4e^- \rightarrow 2H_2O \quad (7)$$

The surface zeta potential values of various samples are displayed in Fig. 7. As pH value of KCl electrolyte increased, zeta potential of all the samples tended to decrease. When pH value was 7.4, all the surfaces were negatively charged, and the values of Ti, C–Ti, Cu–Ti and C/Cu–Ti were −76.7 mV, −104.6 mV, −59.6 mV and −50.9 mV, respectively. Zeta potential of C–Ti sample was more negative than that of Ti, which may be related to the existence of amorphous carbon on such simple surface. The combination of carbon atoms in amorphous carbon

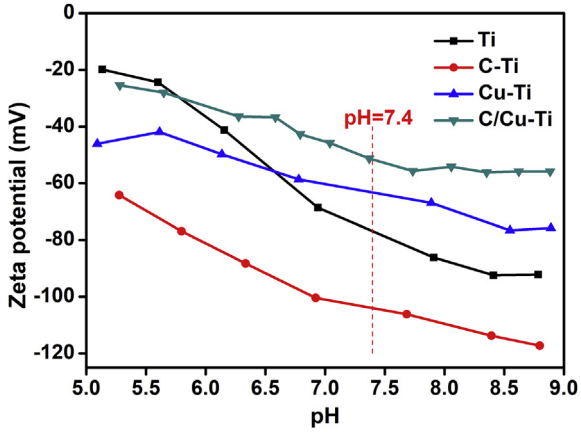

Fig. 7. Surface zeta potential values of different samples at various pH values.

included both SP^3 hybridization and SP^2 hybridization of carbon atoms [64]. Therefore, C–Ti surface contained negatively charged free electrons, which may cause the zeta potential of C–Ti surface to be lower than that of Ti surface. Zeta potential value of C/Cu–Ti surface was slightly positive than that of Cu–Ti. The reason may be that more copper ions with positive charges were released from C/Cu–Ti surface at pH 7.4. (The zeta potential values of Ti surface cited data from previous studies [30]).

Fig. 8 displays nano-hardness curves of the sample surfaces. Surface hardness of samples with ion implantation tended to increase in comparison with pure Ti, especially for C/Cu–Ti and C–Ti samples, which may be caused by high hardness of TiC on their surfaces. Copper implantation could slightly increase the nano-hardness value of Ti surface, possibly because of the existence of interior metallic copper [65].

The curves in nano-hardness of surfaces of the samples with depth are exhibited in Fig. 9. In general, nano-hardness value of C/Cu–Ti was the largest, rising to the peak at 22 nm (about 13 Gpa), before dropping generally to around 9 Gpa at 60 nm. And nano-hardness values of Cu–Ti and C–Ti were larger than that of Ti, so the nano-hardness value of Ti surface could be increased significantly by carbon/copper ions co-implantation, and the result was consistent with the trend showed in Fig. 8. (The nano-hardness data of Ti surface cited data from previous studies [30]).

3.3. Antibacterial ability

The antibacterial ability of different samples against *E. coli* and *S. aureus* was quantitatively studied through plate counting method. The number of bacterial colonies on C–Ti or Ti was evidently more than that on C/Cu–Ti or Cu–Ti (Fig. 10a and b). According to Fig. 10c and d,

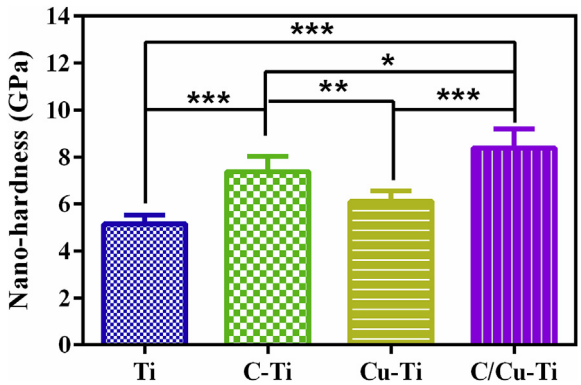

Fig. 8. Hardness average values of various samples at the depth from 40 nm to 60 nm.

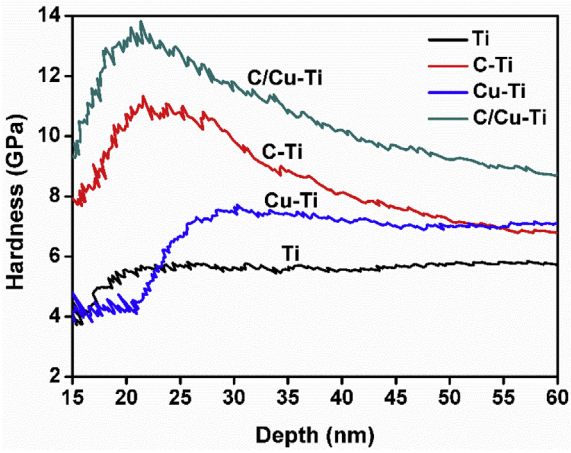

Fig. 9. Nano-hardness curves of various samples.

inhibition rates to *S. aureus* and *E. coli* on surface of C–Ti were about 20% and 10%, respectively, indicating the weak antibacterial ability of C–Ti. This phenomenon would be explained below in conjunction with SEM morphologies of bacteria. The percent reductions of *E. coli* on both surfaces of Cu–Ti and C/Cu–Ti were about 100%. On the other hand, antibacterial rate of C/Cu–Ti against *S. aureus* was about 90%, and that of Cu–Ti was 75%. The results demonstrated that antibacterial properties of C/Cu-Ti were superior to the single Cu ion implantation (Cu–Ti).

Figs. 11 and 12 show SEM morphologies of *E. coli* and *S. aureus* after 24h cultivation on various surfaces. On pure Ti surface, a large number of *E. coli* and *S. aureus* grew well, while the number of bacteria on C–Ti surface was slightly decreased. The adhesion of bacteria on the material surface mainly includes 2 stages: at the first stage, the initial physical and chemical interaction happens; the second stage is the interaction of molecules and bacteria [66]. Among the various interface parameters of materials, surface roughness and chemical composition are considered as two important factors related to the interaction between materials and bacteria. Before and after C-PIII&D modification, the sample's surface morphology did not show obvious change. Therefore, the surface roughness of the sample had negligible effect on bacteria adhesion, and bacteria adhesion was mainly controlled by the chemical composition of sample surface. According to the XPS results, the main component of the surface modified by C-PIII&D was amorphous carbon, which was chemically inert. It weakened the chemical action of the sample and bacteria, thus inhibited bacterial adhesion [26,27]. Secondly, according to Fig. 7, the zeta potential value of C–Ti was lower than that of pure Ti sample at pH 7.4. Since bacterial membrane was negatively charged, C–Ti sample inhibited bacterial adhesion due to a stronger electrostatic repulsion. Therefore, the inhibition of bacterial adhesion by carbon ion implantation samples was considered to be the result of the combination of the larger chemical inertness of the surface carbon film and the negative surface potential. As shown in Fig. 11, compared with Ti and C–Ti, fewer complete bacterial individuals were found on both surfaces of Cu–Ti and C/Cu–Ti, and most *E. coli* had been split and dead, which indicated good antibacterial properties of those surfaces against *E. coli*.

In Fig. 12, a large number of *S. aureus*, which grew well and had spherical shape, existed on Ti surface. However, some of the *S. aureus* with obvious dryness and flatness shape were on Cu–Ti. Moreover, more membranes of *S. aureus* on C/Cu–Ti were damaged, indicating that C/Cu dual ions implantation showed good antibacterial effect against *S. aureus*. The results above were consistent with the previous results shown in Fig. 10.

3.4. Cytotoxicity

Fig. 13 exhibits proliferation activity of mouse osteoblast MC3T3-E1 on different sample surfaces. It can be seen that cell activities on Cu–Ti and C/Cu–Ti were slightly higher than those on Ti and C–Ti, and this can be ascribed to the small amount of released copper ions. In our

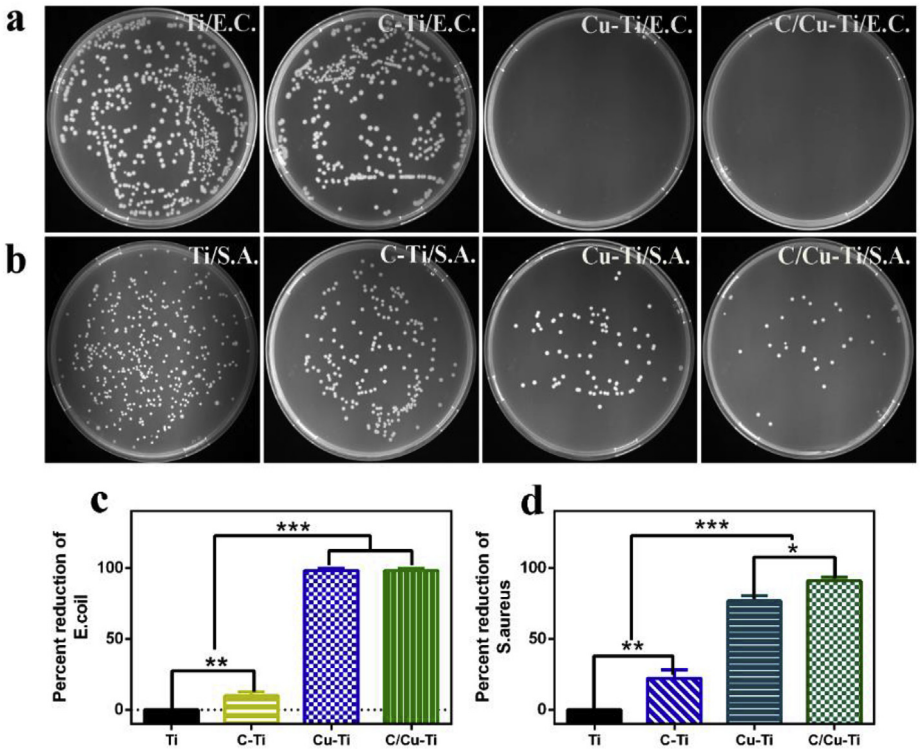

Fig. 10. Images of *E. coli* and *S. aureus* colonies on surfaces of different samples: *E. coli* (a) and *S. aureus* (b); Percent reductions of bacteria re-cultivated on agar: *E. coli* (c) and *S. aureus* (d). (*$p < 0.05$, **$p < 0.01$, ***$p < 0.001$).

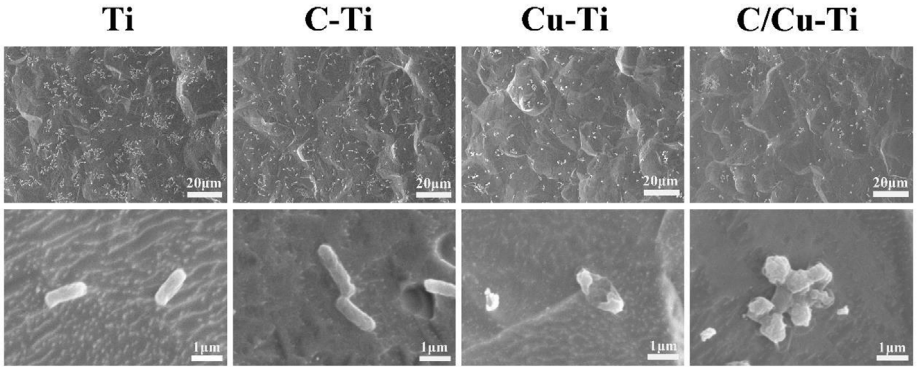

Fig. 11. SEM morphology of *E. coli* seeded on different surfaces after incubation for 24 h.

previous study, we have investigated the dose-response relationship between copper and its biocompatibilities, and the results showed that copper ions can stimulate the proliferation of MC3T3-E1 within the concentration of about 12.34 μM (0.8 ppm) [67]. As shown in Fig. 5, the accumulated concentration of copper ions for Cu–Ti and C/Cu–Ti is less than 0.2 ppm after 14 days incubation, indicating Cu–Ti and C/Cu–Ti have good cytocompatibility to MC3T3-E1.

Schematic diagram of possible antibacterial mechanism on the surface of C/Cu co-implanted titanium is shown in Fig. 14. Amorphous carbon with chemical stability existed and the standard electrode potential of titanium dioxide is significantly more negative than that of copper, so Cu phase tends to serve as an anode releasing Cu^{2+}, and amorphous carbon serves as a cathode. As a result, more Cu^{2+} could be released from the C/Cu–Ti surface than those from Cu–Ti surface. Burghardt et al. revealed that copper ions are not cytotoxic and could effectively kill bacteria, if its concentration is controlled within 10 mg/L [68]. In this experiment, there is less than 10 mg/L Cu^{2+} released from Cu–Ti and C/Cu–Ti, and more copper ions within the save limitation can thus enter the microenvironment between the sample's surface and bacteria to improve its antibacterial ability.

Besides, carbon acts as the cathode where a hydrogen evolution reaction and a reduction of dissolved oxygen take place, and these reactions can consume hydrogen ions (protons) in the microenvironment. Proton concentration ladder inside and outside the bacterial cell membrane is then affected [28]. The reduction of proton outside membrane will inevitably affect the process of ATP synthesis where protons transported from the outside of membrane are needed, which may cause bacteria to have insufficient energy and eventually lead to bacterial death [61]. “Synergistic effect” brought by C/Cu dual ions implantation can display good antibacterial effects without causing cytotoxicity.

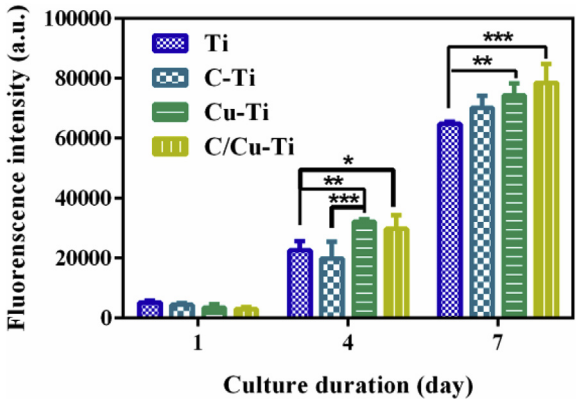

Fig. 13. Proliferative activity of MC3T3-E1 cultured on various surfaces for several days.

4. Conclusion

After C/Cu co-implantation, titanium surface mainly contained amorphous carbon and copper-bearing nano-particles, and TiC phase existed in near surface layer. C/Cu ions implantation could improve mechanical properties of Ti surface, which was mainly attributed to the effect of TiC phase. C/Cu ions implanted Ti surface could form Cu/C galvanic corrosion pairs, in which Cu served as anode, and C acted as cathode, thereby protecting the Ti surface and improving anti-corrosion performance of Ti surface. Copper ion release was controlled and resistance of Ti surface to bacteria was effectively improved by effect of galvanic corrosion, and Ti surface was free of cytotoxicity after C/Cu ions were implanted.

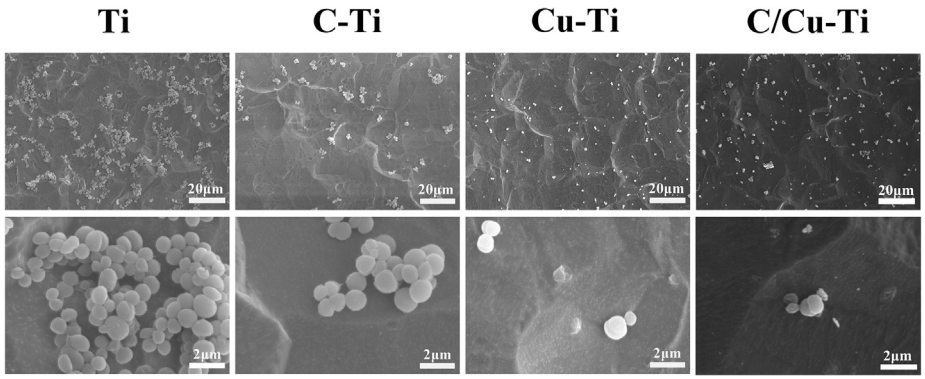

Fig. 12. SEM morphology of *S. aureus* seeded on different surfaces after incubation for 24 h.

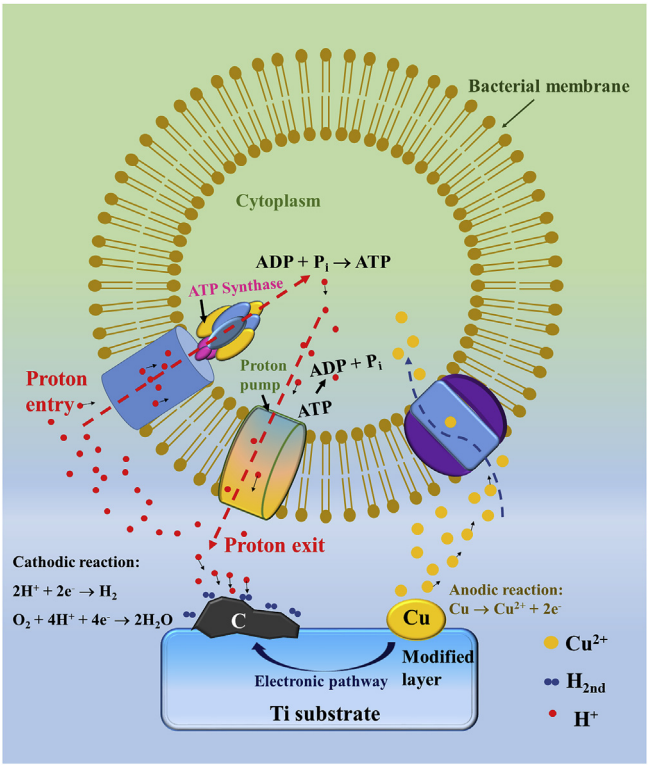

Fig. 14. Schematic diagram of possible antibacterial mechanism on titanium surface after C/Cu co-implantation.

Declaration of competing interest

None.

Acknowledgements

Financial support from the National Key Research and Development Program of China (2016YFC1100604), National Natural Science Foundation of China (31570973, 31870944 and 51831011), Science and Technology Commission of Shanghai Municipality (19JC1415500), Science Foundation for Youth Scholar of State Key Laboratory of High Performance Ceramics and Superfine Microstructures (SKL201606) are acknowledged.

References

[1] G. Hooper, The ageing population and the increasing demand for joint replacement, N. Z. Med. J. 126 (1377) (2013) 5.
[2] Gang Shen, Ju-Fan Zhang, Feng-Zhou Fang, In vitro evaluation of artificial joints: a comprehensive review, Adv. Manuf. (2019).
[3] Ji Li, Ketao Wang, Zhongli Li, et al., Mechanical tests, wear simulation and wear particle analysis of carbon-based nanomultilayer coatings on Ti 6 Al 4 V alloys as hip prostheses, RSC Adv. 8 (13) (2018) 6849–6857.
[4] Liu X, Chu P K, Ding C. Surface modification of titanium, titanium alloys, and related materials for biomedical applications[J]. Mater. Sci. Eng. Rep., 47(3):49-121.
[5] S.R. Ge, Q.L. Wang, Investigation on the biotribology of the modified artificial joint materials, J. Med. Biomech. (2009).
[6] J. Raphel, J. Karlsson, S. Galli, et al., Engineered protein coatings to improve the osseointegration of dental and orthopaedic implants, Biomaterials 83 (2016) 269–282.
[7] L. Peddi, R.K. Brow, R.F. Brown, Bioactive borate glass coatings for titanium alloys, J. Mater. Sci. Mater. Med. 19 (9) (2008) 3145–3152.
[8] R.J. Solar, S.R. Pollack, E. Korostoff, In vitro corrosion testing of titanium surgical implant alloys: an approach to understanding titanium release from implants, J. Biomed. Mater. Res. 13 (2) (1979) 217–250.
[9] J. Pan, C. Leygraf, D. Thierry, et al., Corrosion resistance for biomaterial applications of TiO_2 films deposited on titanium and stainless steel by ion-beam-assisted sputtering, J. Biomed. Mater. Res. 35 (3) (1997) 309–318.
[10] J. Wang, J. Li, S. Qian, et al., Antibacterial surface design of titanium-based biomaterials for enhanced bacteria-killing and cell-assisting functions against periprosthetic joint infection, ACS Appl. Mater. Interfaces (2016).
[11] L. Joska, J. Fojt, L. Cvrcek, et al., Properties of titanium-alloyed DLC layers for medical applications, Biomatter 4 (1) (2014) e29505.
[12] M. Allen, B. Myer, N. Rushton, In Vitro and in vivo investigations into the biocompatibility of Diamond-Like carbon (DLC) coatings for Orthopedic Applications, J. Biomed. Mater. Res. 58 (3) (2001) 319–328.
[13] M.H. Ahmed, J.A. Byrne, Effect of surface structure and wettability of DLC and N-DLC thin films on adsorption of glycine, Appl. Surf. Sci. 258 (12) (2012) 5166–5174.
[14] R. Paul, R.N. Gayen, S. Hussain, et al., Synthesis and characterization of composite films of silver nanoparticles embedded in DLC matrix prepared by plasma CVD technique, Eur. Phys. J. Appl. Phys. 47 (1) (2009) 10502.
[15] K. Lukaszkowicz, J. Sondor, K. Balin, et al., Characteristics of CrAlSiN + DLC coating deposited by lateral rotating cathode arc PVD and PACVD process, Appl. Surf. Sci. 312 (2014) 126–133.
[16] Y. Oka, M. Kirinuki, T. Suzuki, et al., Effect of ion beam implantation on density of DLC prepared by plasma-based ion implantation and deposition, Nucl. Instrum. Methods Phys. Res. B 242 (1–2) (2006) 335–337.
[17] K. Baba, R. Hatada, Preparation and properties of nitrogen and titanium oxide incorporated diamond-like carbon films by plasma source ion implantation, Surf. Coating. Technol. 136 (1–3) (2001) 192–196.
[18] F. Meng, Z. Li, X. Liu, Synthesis of tantalum thin films on titanium by plasma immersion ion implantation and deposition, Surf. Coating. Technol. 229 (2013) 205–209.
[19] G. Jin, H. Cao, Y. Qiao, et al., Osteogenic activity and antibacterial effect of zinc ion implanted titanium, Colloids Surf. B Biointerfaces 117 (9) (2014) 158–165.
[20] Y. Zhao, S.M. Wong, H.M. Wong, et al., Effects of carbon and nitrogen plasma immersion ion implantation on in vitro and in vivo biocompatibility of titanium alloy, ACS Appl. Mater. Interfaces 5 (4) (2013) 1510–1516.
[21] R. Poon, K. Yeung, X. Liu, et al., Carbon plasma immersion ion implantation of nickel-titanium shape memory alloys, Biomaterials 26 (15) (2005) 2265–2272.
[22] J.H. Sui, Z.Y. Gao, W. Cai, et al., DLC films fabricated by plasma immersion ion implantation and deposition on the NiTi alloys for improving their corrosion resistance and biocompatibility, Mater. Sci. Eng. 454 (16) (2007) 472–476.
[23] Chao Xia, Shi Qian, Donghui Wang, et al., Properties of carbon ion implanted biomedical titanium, Acta Metall. Sin. 53 (10) (2017) 1393–1401.
[24] O. Sharifahmadian, H.R. Salimijazi, M.H. Fathi, J. Mostaghimi, L. Pershin, Relationship between surface properties and antibacterial behavior of wire arc spray copper coatings, Surf. Coating. Technol. 233 (2013) 74–79.
[25] O. Akhavan, E. Ghaderi, Cu and CuO nanoparticles immobilized by silica thin films as antibacterial materials and photocatalysts, Surf. Coating. Technol. 205 (1) (2010) 219–223.
[26] J. Wang, N. Huang, P. Yang, et al., The effects of amorphous carbon films deposited on polyethylene terephthalate on bacterial adhesion, Biomaterials 25 (16) (2004) 3163–3170.
[27] J. Wang, C.J. Pan, P. Li, et al., Antibacterial properties of amorphous carbon films deposited on polyethylene terephthalate by C_2H_2 plasma immersion ion implantation-deposition, J. Funct. Mater. 35 (5) (2004) 563–565.
[28] H. Cao, X. Liu, F. Meng, P.K. Chu, Biological actions of silver nanoparticles embedded in titanium controlled by micro-galvanic effects, Biomaterials 32 (2011) 693.
[29] L. Yu, G. Jin, L. Ouyang, et al., Antibacterial activity, osteogenic and angiogenic behaviors of copper-bearing titanium synthesized by PIII&D, J. Mater. Chem. B 4 (7) (2016) 1296–1309.
[30] Chao Xia, Dingsen Cai, Ji Tan, et al., Synergistic effects of N/Cu dual ions implantation on stimulating antibacterial ability and angiogenic activity of titanium, ACS Biomater. Sci. Eng. 4 (2018) 3185–3193.
[31] M. Shakerzadeh, H.T.Edwin Teo, C.W. Tan, B.K. Tay, Superhydrophobic carbon nanotube/amorphous carbon nanosphere hybrid film, Diamond and Related Materials 18 (10) (2009) 1235–1238.
[32] J. Hrbek, Carbonaceous overlayers on Ru(001), J. Vac. Sci. Technol. Vac. Surface. Films 4 (1) (1986) 86–89.
[33] H. Ihara, Y. Kumashiro, A. Itoh, et al., Some aspects of ESCA spectra of single crystals and thin films of titanium carbide, Jpn. J. Appl. Phys. 12 (9) (1973) 1462–1463.
[34] C. Gaillard, M.A. Lepez-Heredia, G. Legeay, P. Layrolle, Raio Frequency Plasma Treatments on Titanium for Enhancement of Bioactivity, Acta Biomaterialia 4 (6) (2008) 1953–1962.
[35] G. Schön, ESCA studies of Cu, Cu_2O and CuO, Surf. Sci. 35 (1) (1973) 96–108.
[36] A.C. Miller, G.W. Simmons, Copper by XPS, Surf. Sci. Spectra 2 (1) (1993) 55–60.
[37] T. Nakamura, H. Tomizuka, M. Takahashi, et al., Methods of powder sample mounting and their evaluations in XPS analysis, Hyomen. Kagaku 16 (8) (1995) 515–520.
[38] J.G. Jolley, G.G. Geesey, M.R. Hankins, et al., Auger electron and X-ray photoelectron spectroscopic study of the biocorrosion of copper by alginic acid polysaccharide, Appl. Surf. Sci. 37 (4) (1989) 469–480.
[39] F. Parmigiani, G. Pacchioni, F. Illas, et al., Studies of the Cu-O bond in cupric oxide by X-ray photoelectron spectroscopy and ab initio electronic structure models, J. Electron. Spectrosc. Relat. Phenom. 59 (3) (1992) 255–269.
[40] R.J. Bird, P. Swift, Energy calibration in electron spectroscopy and the re-determination of some reference electron binding energies, J. Electron. Spectrosc. Relat. Phenom. 21 (3) (1980) 227–240.
[41] A.C. Miller, G.W. Simmons, Copper by XPS, Surf. Sci. Spectra 2 (1) (1993) 55–60.
[42] M.P. Seah, M.T. Anthony, Quantitative XPS: the calibration of spectrometer intensity-energy response functions-the establishment of reference procedures and instrument behaviour, Surf. Interface Anal. 6 (5) (1984) 230–241.

[43] A.P. Dementjev, O.P. Ivanova, L.A. Vasilyev, et al., Altered layer as sensitive initial chemical state indicator, J. Vac. Sci. Technol. Vac. Surface. Films 12 (2) (1994) 423–427.
[44] R. Sanjines, H. Tang, H. Berger, et al., Electronic structure of anatase TiO_2 oxide, J. Appl. Phys. 75 (6) (1994) 2945.
[45] D. Gonbeau, C. Guimon, G. Pfister-Guillouzo, et al., XPS study of thin films of titanium oxysulfides, Surf. Sci. 254 (1–3) (1991) 81–89.
[46] Z.N. Wan, R. Cai, S.M. Jiang, Z.P. Shao, Nitrogen- and TiN-modified $Li_4Ti_5O_{12}$: one-step synthesis and electrochemical performance optimization, Journal of Materials Chemistry 22 (2012) 17773–17781.
[47] D.M. Devia, E.R. Parra, P.J. Arango, Comparative study of titanium carbide and nitride coatings grown by cathodic vacuum arc technique, Applied Surface Science 258 (3) (2011) 1164–1174.
[48] R. Leesungbok, M.H. Lee, N. Oh, S.W. Lee, S.E. Kim, Y.P. Yun, J.H. Kang, Factors influencing osteoblast maturation on microgrooved titanium substrata, Biomaterials 31 (14) (2010) 3804–3815.
[49] E.M. Prehn, I.J. Echols, H.S. An, X.F. Zhao, Z.Y. Tan, M. Radovic, M.J. Green, J.L. Lutkenhaus, pH-Response of polycation/$Ti_3C_2T_x$ MXene layer-by-layer assemblies for use as resistive sensors, Molecular Systems Design & Engineering 5 (2020) 366–375.
[50] H.Z. Ye, X.Y. Liu, H.P. Hong, Cladding of titanium/hydroxyapatite composites onto Ti_6Al_4V for load-bearing implant applications, Materials Science and Engineering 29 (6) (2009) 2036–2044.
[51] J.M. Yassin, O.A. Zelekew, D.H. Kuo, K.E. Ahmed, H. Abdullah, Synthesis of efficient silica supported TiO_2/Ag_2O heterostructured catalyst with enhanced photocatalytic performance, Applied Surface Science 410 (2017) 454–463.
[52] R.P. Netterfield, P.J. Martin, C.G. Pacey, et al., Ion-assisted deposition of mixed TiO_2-SiO_2 films, J. Appl. Phys. 66 (4) (1989) 1805–1809.
[53] A.P. Rao, C.S. Sunandana, Growth and surface morphology of ion-beam sputtered Ti–Ni thin films, Nuclear Instruments and Methods in Physics Research Section B: Beam Interactions with Materials and Atoms 266 (8) (2008) 1517–1521.
[54] X. Ding, G.F. Wang, J.H. Li, K.G. Lv, W.J. Zhang, G.Z. Yang, X.Y. Liu, X.Q. Jiang, Surface thermal oxidation on titanium implants to enhance osteogenic activity and *in vivo* osseointegration, Scientific Reports 6 (2006) 31769.
[55] S.M. Green, D.M. Grant, J.V. Wood, et al., XPS characterisation of surface modified Ni-Ti shape memory alloy, Materials Science and Engineering 224 (1–2) (1997) 21–26.
[56] J.E. Glaub, A.R. Bruke, C.R. Brown, W.C. Bowling, D. Kapsch, C.M. Love, R.B. Whitaker, W.F. Moddeman, Ignition mechanism of the titanium–boron pyrotechnic mixture, Surface and Interface Analysis 11 (6–7) (1988) 353–358.
[57] B.L. Gan, K.H. Leong, S. Ibrahim, P. Saravanan, et al., Synthesis of surface plasmon resonance (SPR) triggered Ag/TiO_2 photocatalyst for degradation of endocrine disturbing compounds, Applied Surface Science 319 (2014) 128–135.
[58] F. Samoila, V. Tiron, I.L. Velicu, M. Dobromir, A. Demeter, C. Ursu, L. Sirghi, Reactive multi-pulse HiPIMS deposition of oxygen-deficient TiO_x thin films, Thin Solid Films 603 (2016) 255–261.
[59] J.Y. Feng, L. Wan, J.F. Li, W. Sun, Z.Q. Mao, Improved optical response and photocatalysis for N-doped titanium oxide (TiO_2) films prepared by oxidation of TiN, Applied Surface Science 253 (10) (2007) 4764–4767.
[60] B. Adeloju, Y.Y. Duan, Corrosion resistance of Cu_2O and CuO on copper surfaces in aqueous media, Br. Corrosion J. 29 (4) (1994) 309–314.
[61] G. Jin, H. Qin, H. Cao, et al., Synergistic effects of dual Zn/Ag ion implantation in osteogenic activity and antibacterial ability of titanium, Biomaterials 35 (27) (2014) 7699–7713.
[62] J. Robertson, Diamond-like amorphous carbon, Mater. Sci. Eng. R Rep. 37 (4-6) (2002) 129–281.
[63] J. Robertson, Amorphous carbon cathodes for field emission display, Thin Solid Films 296 (1–2) (1997) 61–65.
[64] Javier Díaz, G. Paolicelli, S. Ferrer, et al., Separation of the sp^3 and sp^2 components in the C1s photoemission spectra of amorphous carbon films, Phys. Rev. B 54 (11) (1996) 8064–8069.
[65] S. Wang, Z. Ma, Z. Liao, et al., Study on improved tribological properties by alloying copper to CP-Ti and Ti-6Al-4V alloy, Mater. Sci. Eng. C Mater. Biol. Appl. (2015).
[66] Y.H. An, R.J. Friedman, Concise review of mechanisms of bacterial adhesion to biomaterial surfaces, J. Biomed. Mater. Res. 43 (3) (1998) 338–348.
[67] Kunqiang Li, Chao Xia, Yuqin Qiao, Xuanyong Liu, Dose-response relationships between copper and its biocompatibility/antibacterial activities, J. Trace Elem. Med. Biol. 55 (2019) 127–135.
[68] I. Burghardt, Frank Lüthen, C. Prinz, et al., A dual function of copper in designing regenerative implants, Biomaterials 44 (2015) 36–44.